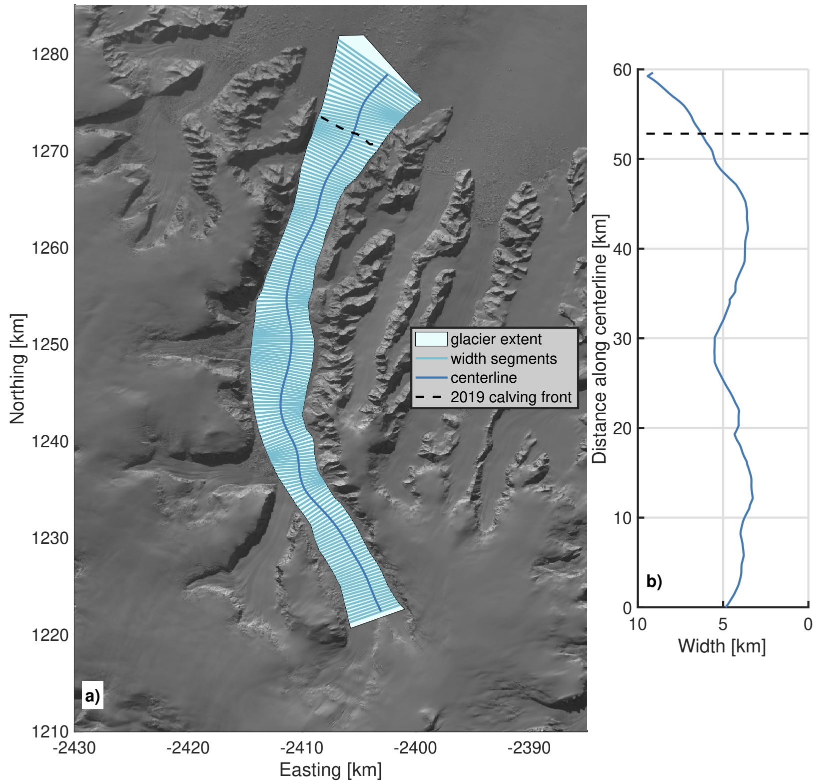

Fig. S1. a) Map view of the glacier extent polygon used to clip line segments perpendicular to the glacier centerline, creating width segments. The background image is a Landsat 8 panchromatic image from 13 October 2019. b) The glacier centerline width profile.

SUPPLEMENTARY MATERIAL

Glacier geometry profiles

Glacier width profile

Figure S1 shows the manually delineated glacier extent and line segments that were used to determine the width along the glacier centerline, as well as to construct the width-averaged glacier geometry and speed profiles.

Glacier bed profile

The bed elevation profile along the glacier centerline was manually delineated from the 2018 NASA OIB level 1B data product (Paden and others, 2014) recorded 16 October 2018 over Crane (Fig. 2) using code adapted from CReSIS (2021). A constant radar velocity and dielectric permittivity (3.15; Evans, 1965) were assumed for ice to convert the travel-time image to range distance. Distances were then referenced with respect to the WGS84 geoid (i.e., orthometric elevations). Gain control was automatically applied to the NASA OIB radar echograms, which were then plotted as distance along the flight line. The image contrast was adjusted so that visual inspection of the plot revealed a distinct echo from the ice surface and ice-bedrock boundary. Once the bed elevation returns were manually selected, a smooth profile was interpolated between the picks using a piecewise cubic hermite interpolating polynomial function. The bed elevation near the ice divide provided by the OIB level 2 data product and sonar-derived fjord bathymetry obtained near the calving front in 2006 (Rebesco and others, 2014) were used to constrain the start and end points of the manually-delineated bed elevation profile (Fig. S2).

Larsen C ice shelf submarine melt rate

The along-flow decrease in melt rate of the floating ice tongue with respect to distance from the grounding line was simulated using the 2010–2018 time-averaged submarine melt rate as computed by Adusumilli and others (2020) for the Larsen C ice shelf. Upon extrapolating the submarine melt rate along six approximately flow-following transects for the Larsen C ice shelf, we computed the submarine melt rate along the floating ice tongue using the spatially-averaged, best fit exponential trend ($\mathrm{R}^2 = 0.77$) as a function of the maximum melt rate and the distance from the grounding line, shown in Figure S3.

Rate and basal roughness factors

To tune the rate factor $A(x)$, which controls the depth-averaged effective viscosity [Pa s], we first calculated $A(x)$ as a function of air temperature using the Arrhenius relationship:

$$A(x) = 3.5 \cdot 10^{-25} e^{-\frac{Q}{RT(x)}} \tag{5}$$

where $T(x)$ is the air temperature [K], Q is the activation energy for creep [$\sim$60$\cdot$10^3 J mol^{-1}], and R is the universal gas constant [8.314 J mol^{-1} K^{-1}] (Cuffey and Paterson, 2010). For $T(x)$, we used the mean annual RACMO air temperature for 1998–2018, adjusted for elevation assuming a dry adiabatic lapse rate of 9.8$\cdot$10^{-3} °C m^{-1}. The temperature-based $A(x)$ was then adjusted to account for strain heating of the ice as it advects towards the calving front (Enderlin and others, 2013a). To do this, strain rates were calculated using width-averaged surface observations of speed along the centerline. Next, the time required for ice to advect between each centerline point (i.e., advection time) was computed from the speed

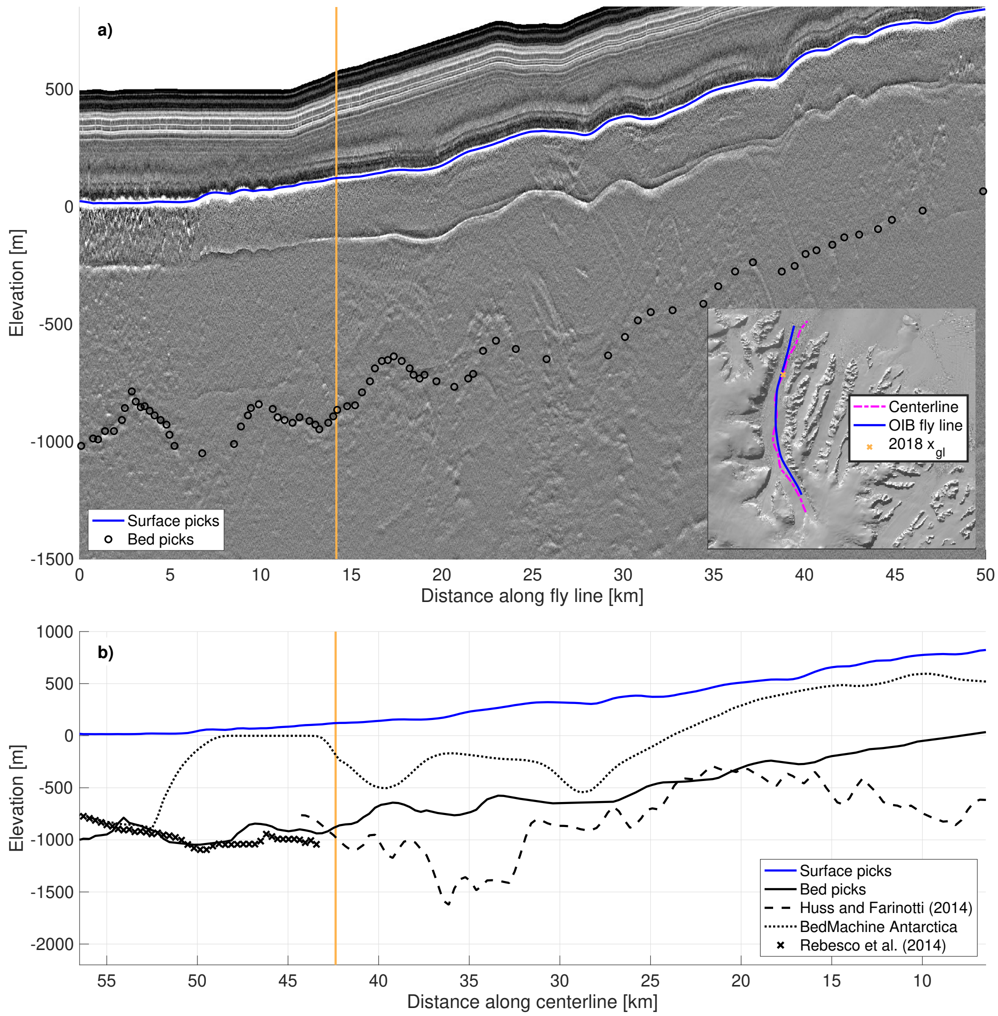

Fig. S2. a) Automatically picked surface elevation and manually picked bed elevation near the glacier centerline from the 2018 NASA OIB level 1B radar echogram recorded 16 October 2018. Inset plot shows a map view of the glacier centerline and the OIB flight path. b) The surface elevation picks and bed picks plotted against bed models from Huss and Farinotti (2014) and BedMachine Antarctica (Morlighem, 2019) and bathymetry observations from Rebesco and others (2014) captured through sonar surveying in 2006. The orange vertical bar in panels a) and b) and the orange cross in the inset plot denote the modeled 2018 grounding line position (x_{gl}).

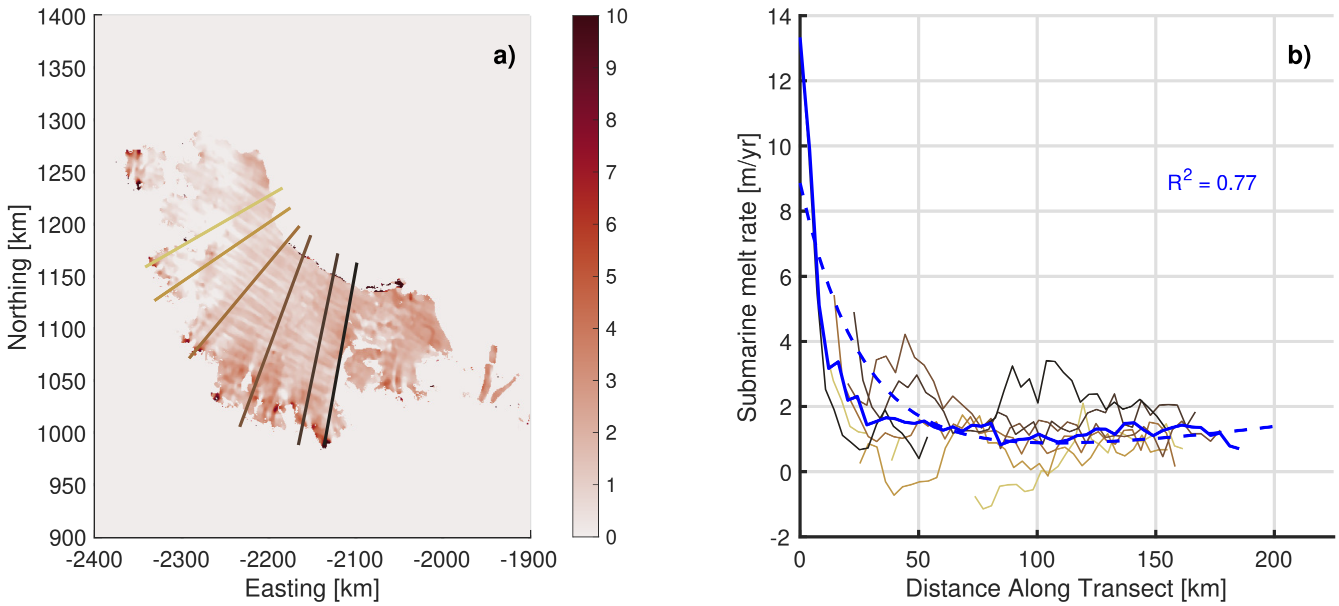

Fig. S3. a) Submarine melt rates for the Larsen C ice shelf time-averaged over 2010–2018 from Adusumilli and others (2020) with six melt rate transects marked. b) Submarine melt rate along each of the six transects shown in panel a), with the mean at each point (solid blue line) and the best exponential function fit (dashed blue line) shown with respect to distance along the transect.

observations. Finally, the strain accumulated between centerline points was calculated as the product of the strain rate and advection time, and then integrated along flow to construct the average strain profile for years 2008–2018 (Fig. S4a). The average strain profile was then normalized from 1 to 2 to create a scalar multiplier analogous to the enhancement factor. The rate factor profile used in the model simulations is the product of the normalized strain profile and the temperature-dependent $A(x)$, as shown in Figure S4 along with the optimal $\beta(x)$ solution.

Sensitivity test results: additional details

The resulting glacier length, grounding line position, thickness, speed, and grounding line discharge in 2100 for each of the future climate perturbation scenarios are provided in Tables S2-S5 below.

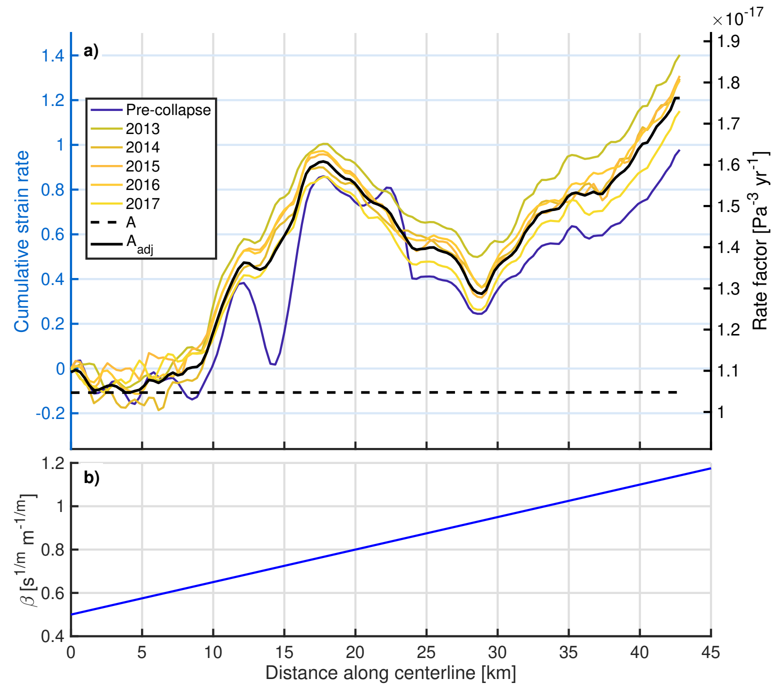

Fig. S4. a) Average annual strain profiles estimated using centerline observations of speed for the pre-ice shelf collapse ("Pre-collapse") and 2013–2017 velocity profiles (left y-axis) and the temperature-dependent rate factor, A, adjusted using the average strain profile, A_{adj} (right y-axis). b) The basal roughness factor, β, tuned so that the pre-ice shelf collapse steady-state model simulation best matched observations of glacier surface elevation and flow speed.

Table S1. Results for the unperturbed scenarios at the final model year 2100, where d_{fw} is the minimum freshwater depth (held constant), ΔL is the change in modeled glacier length, Δx_{gl} is change in the grounding line position along the centerline, and ΔH_{gl}, ΔU_{gl}, and Q_{gl} are the glacier thickness, speed, and mass discharge at the grounding line, respectively, relative to the median d_{fw} scenario.

Minimum d_{fw} **[m]**	ΔL **[km]**	Δx_{gl} **[km]**	ΔH_{gl} **[m]**	U_{gl} **[m yr^{-1}]**	Q_{gl} **[Gt yr^{-1}]**
-5	11.4	0.9	18	-56	1.03
-4	8.5	0.8	15	-48	1.04
-3	4.3	0.6	12	-27	1.07
-2	2.1	0.5	10	-17	1.08
-1	0.9	0.4	7	-10	1.09
0	0.0	0.0	0	0	1.09
1	-1.3	-0.6	-15	26	1.11
2	-2.9	-0.8	-24	48	1.12
3	-4.3	-1	-30	73	1.15
4	-5.7	-1.1	-37	101	1.18
5	-7.4	-1.3	-45	133	1.21

Table S2. Results for the SMB sensitivity tests at the final model year 2100, where ΔSMB is the maximum SMB perturbation near sea level, ΔL is the change in modeled glacier length, Δx_{gl} is change in the grounding line position along the centerline, and ΔH_{gl}, ΔU_{gl}, and Q_{gl} are the glacier thickness, speed, and mass discharge at the grounding line, respectively, with respect to the median unperturbed scenario.

ΔSMB_{max} **[m yr^{-1}]**	ΔL **[km]**	Δx_{gl} **[km]**	ΔH_{gl} **[m]**	U_{gl} **[m yr^{-1}]**	Q_{gl} **[Gt yr^{-1}]**
0.0	0.0	0.0	0	0	1.09
-0.5	-0.4	-0.5	-13	5	1.07
-1.0	-0.9	-0.7	-19	-1	1.05
-1.5	-1.4	-0.8	-25	-3	1.03
-2.0	-2.0	-1.0	-30	-9	1.01
-2.5	-2.5	-1.1	-35	-16	0.99
-3.0	-2.9	-1.2	-39	-21	0.97
-3.5	-3.4	-1.3	-42	-28	0.95
-4.0	-3.8	-1.4	-46	-38	0.92
-4.5	-4.2	-1.4	-49	-49	0.90
-5.0	-4.6	-1.5	-53	-55	0.88

Table S3. Results for the ocean thermal forcing sensitivity tests at the final model year 2100, where $\Delta \mathrm{F}_T$ is the change in ocean thermal forcing with respect to the unperturbed scenario, ΔSMR is the change in submarine melt rate, ΔL is the change in modeled glacier length, Δx_{gl} is change in the grounding line position along the centerline, and ΔH_{gl}, ΔU_{gl}, and Q_{gl} are the glacier thickness, speed, and mass discharge at the grounding line, respectively, with respect to the median unperturbed scenario.

Δ F_T **[°C]**	ΔL **[km]**	Δx_{gl} **[km]**	ΔH_{gl} **[m]**	ΔU_{gl} **[m yr^{-1}]**	Q_{gl} **[Gt yr^{-1}]**
0.0	0.0	0.0	0	0	1.09
0.1	-3.3	-1	-31	77	1.15
0.2	-5.9	-1.3	-43	123	1.2
0.3	-7.5	-1.5	-52	157	1.23
0.4	-8.4	-1.8	-66	186	1.25
0.5	-9.1	-2.2	-79	217	1.28
0.6	-9.9	-2.6	-94	255	1.32
0.7	-10.7	-3.1	-109	305	1.37
0.8	-11.5	-3.4	-119	353	1.41
0.9	-12.3	-3.6	-130	398	1.44
1.0	-13.0	-3.8	-138	434	1.47

Table S4. Results for the submarine melt-enhance SMB sensitivity tests, SMB_{enh}, at the final model year 2100, where ΔSMB_{enh} is the maxmimum surface mass balance perturbation near sea level, ΔL is the change in modeled glacier length, Δx_{gl} is change in the grounding line position along the centerline, and ΔH_{gl}, ΔU_{gl}, and Q_{gl} are the glacier thickness, speed, and mass discharge at the grounding line, respectively.

ΔSMB_{enh} [m yr^{-1}]	ΔL [km]	Δx_{gl} [km]	ΔH_{gl} [m]	ΔU_{gl} [m yr^{-1}]	Q_{gl} [Gt yr^{-1}]
0.0	0.0	0.0	0	0	1.09
-0.5	-2.8	-1.0	-32	29	1.07
-1.0	-4.2	-1.3	-42	29	1.04
-1.5	-5.2	-1.5	-50	11	1.00
-2.0	-6.4	-1.7	-60	5	0.97
-2.5	-7.1	-2.0	-73	-13	0.92
-3.0	-7.7	-2.5	-91	-26	0.89
-3.5	-8.1	-3.2	-113	-30	0.85
-4.0	-8.5	-3.6	-127	-36	0.81
-4.5	-8.9	-3.9	-141	-49	0.77
-5.0	-9.4	-4.3	-155	-42	0.76

Table S5. Results for the concurrent SMB_{enh} and F_T perturbation sensitivity tests at the final model year 2100, where ΔSMB_{enh} is the maximum surface mass balance perturbation near sea level, ΔF_T is the change in ocean thermal forcing, ΔL is the change in modeled glacier length, Δx_{gl} is change in the grounding line position along the centerline, and ΔH_{gl}, ΔU_{gl}, and Q_{gl} are the glacier thickness, speed, and mass discharge at the grounding line, respectively.

ΔSMB_{enh} [m yr^{-1}]	$\Delta \mathbf{F}_T$ [°C]	ΔL [km]	Δx_{gl} [km]	ΔH_{gl} [m]	ΔU_{gl} [m yr^{-1}]	Q_{gl} [Gt yr^{-1}]
0.0	0.0	0.0	0.0	0	0	1.09
-0.5	0.1	-5.9	-1.4	-47	97	1.14
-1.0	0.2	-8.4	-2.3	-84	132	1.14
-1.5	0.3	-10.3	-3.4	-119	210	1.2
-2.0	0.4	-12.4	-4.3	-153	301	1.23
-2.5	0.5	-14.3	-4.9	-174	378	1.27
-3.0	0.6	-16.1	-5.8	-212	462	1.29
-3.5	0.7	-17.5	-6.6	-247	545	1.31
-4.0	0.8	-19.3	-7.5	-279	727	1.43
-4.5	0.9	-20.8	-8.5	-301	682	1.28
-5.0	1.0	-20.3	-8.0	-292	671	1.32